

---

# Chemical origins of fast-charge performance in disordered carbon anodes

---

Sunyhik Ahn<sup>1†</sup>, Marco Lagnoni<sup>2†</sup>, Yi Yuan<sup>3</sup>, Anton Ogarev<sup>1</sup>, Elena Vavrinyuk<sup>1</sup>, George Voynov<sup>1</sup>, Eleanor Barrett<sup>1</sup>, Alexander Pelli<sup>1</sup>, Alexander Atrashchenko<sup>1</sup>, Alexei Platonov<sup>1</sup>, Sergey Gurevich<sup>1</sup>, Maksim Gorokhov<sup>1</sup>, Dmitry Rupasov<sup>1</sup>, Alex W. Robertson<sup>4</sup>, Robert A. House<sup>3</sup>, Lee Johnson<sup>5</sup>, Antonio Bertei<sup>2</sup>, and Denis Chernyshov<sup>1\*</sup>

<sup>1</sup>HE Carbon Supercap Ltd, 32 Telford way, London, U.K.

<sup>2</sup>Department of Civil and Industrial Engineering, University of Pisa, Pisa, Italy

<sup>3</sup>Department of Materials, University of Oxford, Oxford, U.K.

<sup>4</sup>Department of Physics, University of Warwick, Warwick, U.K.

<sup>5</sup>Nottingham Applied Materials and Interfaces Group, School of Chemistry, University of Nottingham, Nottingham, U.K.

<sup>†</sup>These authors contributed equally

\*Corresponding author

To be submitted to ?

## **Abstract**

Fast-charging lithium-ion batteries often cause capacity loss and limited cycle life, hindering their use in high-power applications. Our study employs electrochemical analysis and a multi-physics model to identify and quantify chemical and physical constraints during fast-charging, comparing state-of-the-art graphite and nanocluster carbon (a disordered carbon) anodes. The combination of modelling material phase separation phenomena together with coupled ion-electron transfer theory reveal significant insight. The active material strongly influences charge transfer kinetics and solid-state lithium diffusion. Unlike graphite, nanocluster carbon supports lithium insertion without phase separation, enabling faster lithium diffusion, better volume utilization and lower charge transfer resistance. We demonstrate practical implications of these material phenomena through multi-layer pouch cells made with nanocluster carbon anodes, which withstand over 5,000 fast-charge cycles at 2C without significant degradation ( $< 10\%$  at reference 0.2C).

## **Introduction**

Demand for Li-ion batteries continues to grow exponentially, mainly fuelled by electrification of vehicles and consumer electronics. It is widely recognised that fast-charge batteries that can be charged from 0 to 100% in 30 minutes or less are not only highly desirable but, in the case of electric vehicles, necessary for mass adoption.<sup>1</sup> The challenge with achieving fast-charge performance lies with the sluggish mass transport and kinetic factors that require an overpotential to be applied. This overpotential causes the cell to reach the Li plating voltage limit (where the charging must be stopped) before complete lithium intercalation has occurred, resulting in incomplete utilisation of the anode's capacity. Uneven lithium intercalation also increases the risk of parasitic processes such as Li plating and solid-electrolyte interface aging.<sup>2,3</sup> Hence there is an unfavourable trade-off between fast-charging and capacity retention.

Artificial graphite, the state-of-the-art anode material, has limited fast-charge performance and must be fast charged at elevated temperatures,<sup>4,5</sup> which incurs additional energy and battery pack design costs. While the overall performance of the cell is dependent on a combination of mass transport, kinetics and cell design parameters,<sup>6-9</sup> it has been found that fast-charge capability is significantly impacted by physical-chemical phenomena which are specific to the active material upon lithiation. In particular, phase-separation phenomena, where lithiated graphite forms distinct phases, make graphite particularly poor at fast-charge in terms of capacity retained and cell degradation.<sup>10,11</sup> Prior work have shown that disordered carbon anodes are well suited for fast charge as they retain high capacity at high charging rates as well as resisting lithium plating.<sup>12-16</sup> While there are interesting studies on the intercalation mechanism in disordered carbons,<sup>14,15,17-19</sup> a comprehensive breakdown of the physical processes that explain the differences in performance compared to graphitic electrodes has not been provided to date.

We explain the chemical and physical origins of fast-charge performance by combining experiments with multi-physics modelling. We find that disordered carbons intrinsically facilitate faster solid-state lithium diffusion which, coupled to a lack of phase separation, enables more homogeneous lithiation compared to graphite, leading to improved volume utilisation and charging rate performance. Practical implications of these material phenomena are demonstrated through multi-layer pouch cells made with nanocluster carbon anodes, which show less than 10% capacity loss in reference conditions over 5,000 repetitive fast-charge/discharge cycles at 2C.

## Results & Discussion

The experimental charging rate performance of graphite and nanocluster carbon (nC), a disordered carbon anode, are compared in Fig. 1A and B, where half cells in coin cell setup vs. Li metal are charged (i.e., lithiated) under constant current (CC) mode. The two electrodes have different geometrical and microstructural properties, which are summarised in Tab. S1, in particular different mass loadings (5.8 mg/cm<sup>2</sup> for graphite, 6.9 mg/cm<sup>2</sup> for nC); thus, the electrodes have different theoretical areal capacities (2.04 mAh/cm<sup>2</sup> for graphite, 3.35 mAh/cm<sup>2</sup> for nC) calculated on the basis of the specific capacities measured in quasi-equilibrium conditions (see Fig. S4D), which are also used to define the C-rates (see also Tab. S8). Fig. 1A and B show that graphite is charged and discharged at lower average voltages than nC; on the other hand, nC enables larger accessible specific capacities compared to graphite. Fig. 1C shows the rated capacity as a function of C-rate, where the accessible capacity is normalised to the capacity at 0.2C. Fig. 1C indicates that while the two anode materials retain similar relative capacities at C-rates smaller than 1C, nC significantly outperforms graphite at higher C-rates, with 32% capacity retention at around 3C compared to only 11% for graphite. nC anode's superior charging-rate performance is even more remarkable given

that the nC electrode utilised here is disadvantaged by higher mass loading and areal capacity compared to the graphite anode; this means that higher current needs to be passed for the same C-rate in the nC electrode, resulting in greater ohmic resistance losses, especially for electrolyte lithium-ion transport within the electrode pores. This points to other factors playing a significant role in driving greater fast-charge performance in nC, which are explored in the rest of this section. Fig. 1D shows the first cycle capacity losses during formation, where charge is consumed to form a stable solid-electrolyte-interface (SEI) layer. Disordered carbon anodes typically exhibit high first cycle losses of 20-40%,<sup>20-23</sup> which is undesirable as this irreversible Li inventory consumption necessitates excess cathode loading, which adds to costs and lowers cell level capacity. nC, unlike typical disordered carbon anodes,<sup>24-26</sup> has much lower first cycle losses of 9%, which is comparable to graphite. This was achieved through a patented production method and a series of thermal, mechanical and chemical treatment.<sup>27</sup>

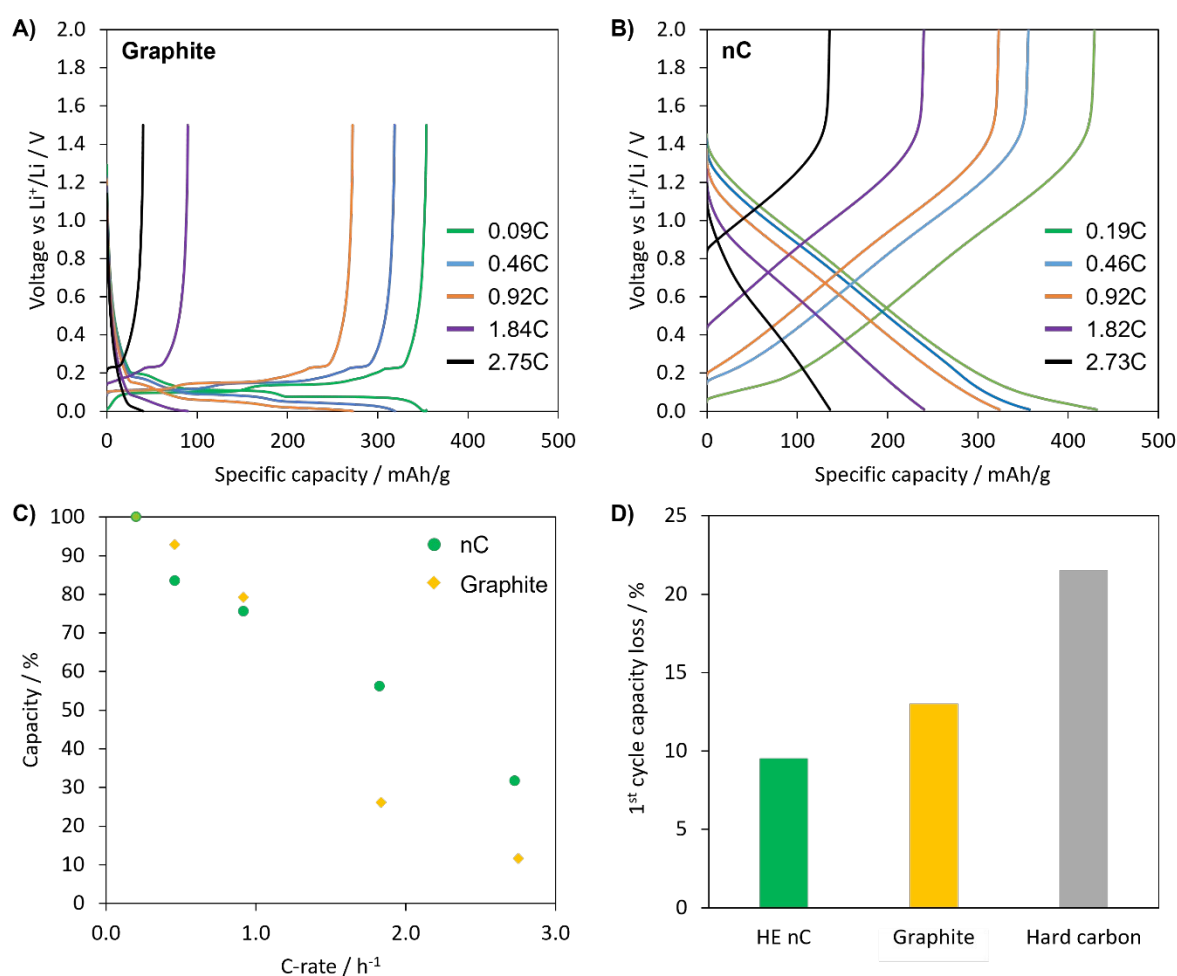


**Fig. 1.** Electrochemical performance of anode half cells: charge and discharge profiles of A) graphite (5.8 mg/cm<sup>2</sup>) and B) nanocluster carbon (nC, 6.9 mg/cm<sup>2</sup>) anodes at varying charging C-rates under constant current mode (refer also Tab. S8 for the currents and C-rates used during charge and discharge). C) Rated capacity upon charge (i.e., lithiation) from A) and B) normalised to the capacity at 0.2C. D) First cycle capacity losses for graphite, hard carbon and nC.

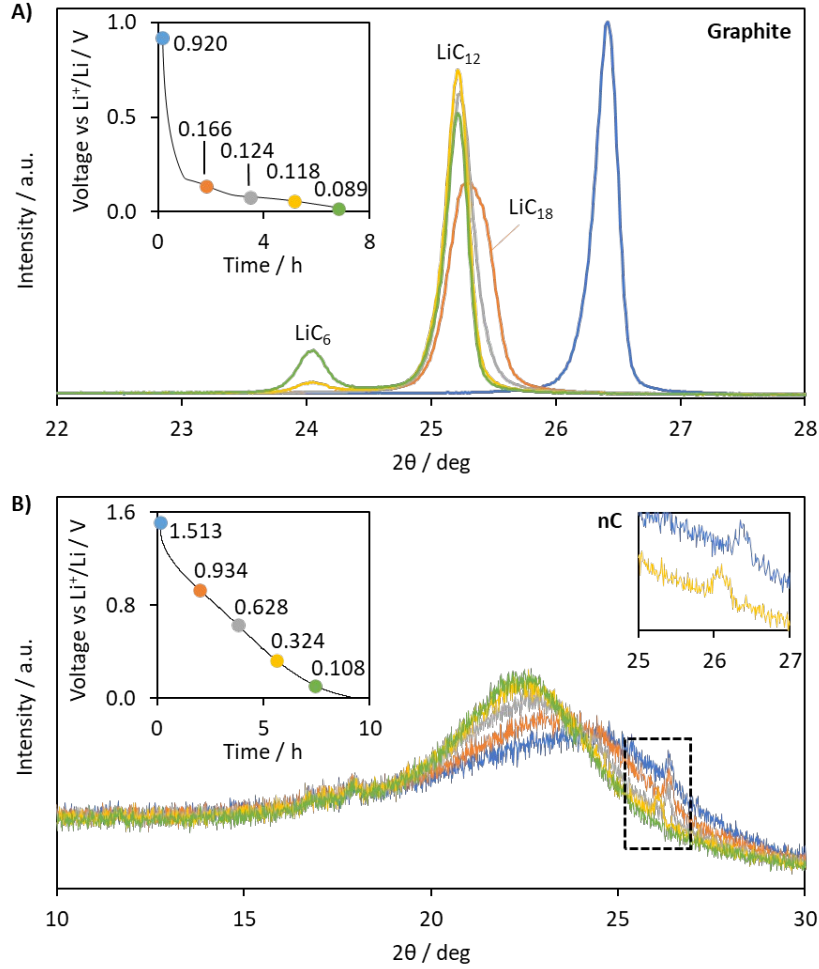


**Fig. 2.** Operando X-ray diffractograms of A) graphite and B) nC during lithiation at C/10 charging rate collected at different operating voltages vs. Li metal, shown in the insets and reporting the colour map.

The anode materials were probed using operando X-ray diffraction (XRD) during lithium intercalation. The formation of distinct lithiated phases shown in Fig. 2A for graphite is well reported in the literature.<sup>17,28</sup> In contrast to this, nC exhibits a single broad peak. The wide breadth of the peak indicates nC exhibits a much shorter correlation length of the stacked layers than in graphite, consistent with the presence of nano-clusters. The peak position shifts to lower angles as a function of increasing states of lithiation (i.e., as the voltage decreases), which indicates gradual expansion of the average inter-layer spacing as lithium intercalates. The continuous change in peak position suggests that lithiation proceeds via a solid solution mechanism consistent with the sloping voltage profile. Unlike graphite, there are no new phases during lithiation for nC nor phase separation in the dominant material XRD peak during lithium intercalation. This is corroborated by the monotonic behaviour of charge/discharge curves for nC shown in Fig. 1B, in contrast to graphite which exhibits voltage plateaus (Fig. 1A), which are more evident in Fig. S4D at open circuit conditions. The smaller peaks visible between 25-27 degrees in Fig. 2B, which match the graphite peaks presented in Fig. 2A, indicate a shift towards lithiated graphite peaks that is evident only when nC has reached 0.324 V (yellow curve in Fig. 2B). According to the voltage-capacity plots in Fig. 1, at such a voltage nC is at ca. 60% state of lithiation whereas graphite is only at around 5%. Li preferentially intercalates into

nC over graphite due to the higher equilibrium potential of the former at the same state of lithiation. Such an intercalation order, which is dictated by the thermodynamics of reduction, has also been observed in other blends of anodes, such as Si-graphite.<sup>29</sup> Therefore, the XRD data in Fig. 2B indicate that nC possesses a minimal fraction of ordering, that is, of graphitic carbon, which intercalates lithium ions only when the majority of the disordered carbon fraction of nC has already undergone lithium intercalation.

Taking these insights from operando XRD, a multi-physics model of the cell is built taking into account electrode microstructural properties such as porosity and tortuosity factor (see Tab. S1) as well as more complex physical-chemical phenomena, such as lithium-induced phase separation in the active material.<sup>30</sup> This model is then fit to experimental CC charge/discharge curves (Fig. S3) and galvanostatic intermittent titration technique (GITT) data (Fig. 3A), where a small current (ca. C/20) is pulsed and relaxed to measure time dependent changes in the voltage. The advantage of utilising our multi-physics model for GITT analysis over conventional analytical approaches based on Weppner-Huggins<sup>31</sup> or Honders<sup>32</sup> methods are that we are not limited to single-phase solid homogeneous films nor solid solution diffusion model approximations.<sup>33,34</sup> These analytical methods are often taken beyond their intended scope to model multi-particle systems with phase-separating materials,<sup>35,36</sup> with some work-arounds to the limiting assumptions.<sup>37-39</sup> The key strength of the physical modelling approach used here is that it models solid-state diffusion according to non-equilibrium thermodynamics,<sup>40</sup> capturing phase-separation behaviour in the case of graphite, in addition to employing a robust theoretical model for coupled ion electron transfer kinetics for lithium (de-)intercalation as opposed to phenomenological Butler-Volmer kinetics.<sup>41</sup> Experimental electrochemical data of graphite and nC electrodes are used to calibrate two physical parameters of the model, namely the solid-state diffusion coefficient of intercalated lithium and the charge transfer kinetic constant at different states of lithiation.

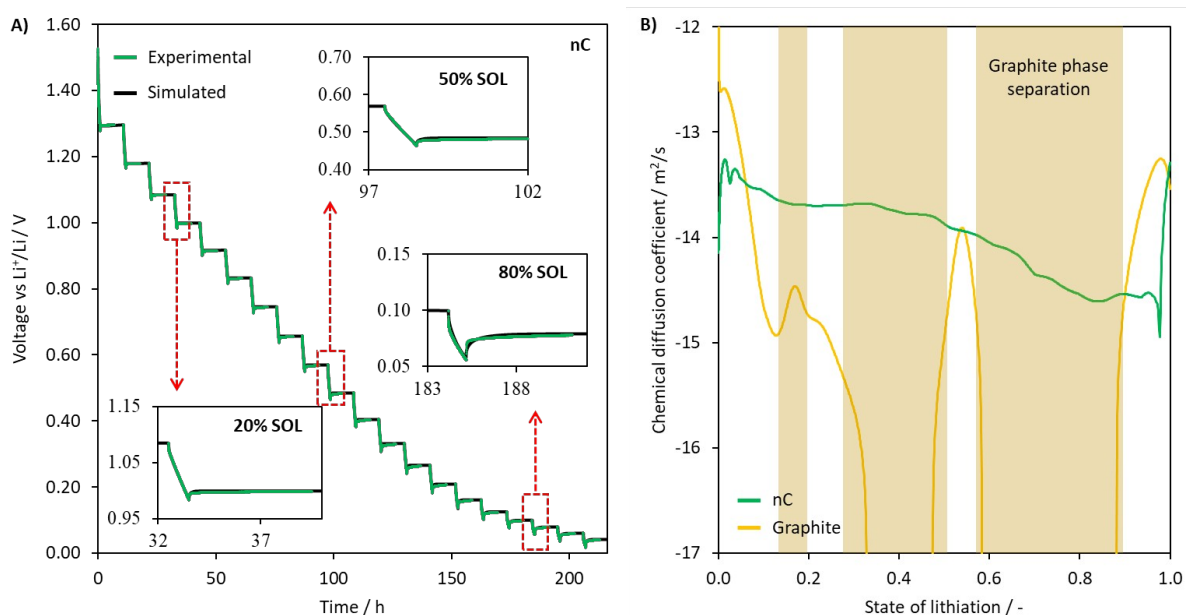


**Fig. 3.** A) GITT measurement experiments and the fitted multi-physics model for nC anode, with insets at various states of lithiation (SOL). B) Estimated lithium chemical diffusion coefficients (in logarithmic scale) for graphite and nC anodes from fitting experiment and simulations from multi-

physics model. The shaded areas indicate the ranges of state of lithiation where graphite is unstable and phase separates into stable phases.

The GITT experiments and the fitted multi-physics modelling results for nC are shown in Fig. 3A; the full set of experimental GITT data is reported in Fig. S4. There is an excellent agreement between model and experiment for nC anode in Fig. 3A, where the model is capable of capturing both the voltage drop during the current pulse as well as the relaxation behaviour upon current interruption. This is corroborated by the good match of CC charge/discharge curves in Fig. S3 for both graphite and nC at different C-rates, indicating that the multi-physics model reproduces the main electrochemical phenomena both during lithiation and de-lithiation even at high current densities.

Simulating the GITT relaxation behaviour of graphite, which undergoes phase separation upon lithiation, is known to be more challenging due to movement of interfaces of stable lithiated phases during equilibration, thus making the voltage response during GITT relaxation too susceptible to the specific particle size distribution of the electrode under investigation.<sup>41,42</sup> For this reason, while the model is calibrated on both GITT and CC charge/discharge data for nC electrode, only the latter are used for the graphite electrode. The overall agreement between simulation and experiment shows that our model successfully captures the essential physical features of both graphite and nC electrodes.

Fig. 3B shows the chemical diffusion coefficient for intercalated lithium within the anode active material estimated from model fitting. The chemical diffusion coefficient in Fig. 3B, useful to compare solid-state diffusion in the two materials in a similar fashion according to Fick law, is derived from the intrinsic diffusion coefficient (Fig. S2), which is obtained from model fitting, as detailed in Eq. (2) of the Materials and methods section. Fig. 3B shows that nC exhibits faster lithium diffusion than graphite for the majority of the state of lithiation window. The trend in diffusion coefficients also differs, with graphite exhibiting large fluctuations which coincide with regions (shaded in Fig. 3B) where phase separation occurs, while nC shows an almost monotonic decrease with state of lithiation. In graphite the formation and separation of lithiated phases may cause significant slowdown in the transport of intercalated lithium, even beyond what can be deduced by looking at the chemical diffusion coefficient only.

At the extremes of these phase separation regions (or states of lithiation), graphite separates into two stable compositions, which have their corresponding chemical diffusion coefficients. By macroscopically probing graphite with GITT or EIS measurement in these regions, one may evaluate an effective value of the chemical diffusion coefficient by using simplified analytical approaches (not originally intended for phase-separating materials)<sup>35,36</sup>. However, such estimates of chemical diffusion coefficient originates from a convolution of the diffusion coefficients of the stable phases as well as from the movement of their interfaces, thus is not truly representative of the diffusion properties of graphite where, in order to account for uphill diffusion, even negative values can be obtained.<sup>35,36</sup> The large spread in reported literature values for graphite spanning 2 orders of magnitude, likely stems from such oversimplified assumptions which likely introduce large errors.<sup>43</sup> Estimated chemical diffusion coefficients for graphite shown in Fig. 3B from our models which take into account phase separation phenomena demonstrate significant differences from those obtained by conventional GITT and EIS methods in the existing literature (Fig. S4E). The only points of agreement between our model estimates and the literature values are within the limited state of lithiation regions where stable graphitic phases exist (see Fig. S4E). That means that for the majority of the state of lithiation window, where there is mix of lithiated graphitic phases, conventional GITT

and EIS methods significantly overestimate the diffusion coefficient by up to 2 orders of magnitude. This overestimation in solid-state lithium mass transport likely leads to underestimating the safety risk of fast-charging lithium-ion batteries. This highlights the importance of accounting for material phase separation physics in analysing and modelling lithium intercalation.

The multi-physics model developed above is further used to interpret the charge-discharge cycling data at variable C-rates in Fig. 1 (refer to SI for model details and microstructure characterization). By fitting the model to faster charging rate data, we are able to quantitatively estimate the overpotentials and capacity losses resulting from limiting factors beyond solid-state diffusion, such as charge transfer resistance and electrolyte resistance. We achieve a good fit between experiment and model as shown in Fig. S3. The modelling results predict the distribution of lithium within the secondary particles (Fig. 4A and B) and at electrode level (Fig. S5) during 2C lithiation. 2D maps of the lithium content within a model secondary carbon particle at the separator at different states during 2C charge are shown as insets together with the charge profile for graphite and nC cells in Fig. 4A and B, respectively. As the inset of Fig. 4A shows, simulations suggest a strong accumulation of intercalated lithium at the surface of graphite particles during 2C lithiation, which has the potential to adversely affect charge transport resistances and increase the risk of Li plating. Concurrently, the core of graphite particles remains underutilised due to limitations on solid-state lithium transport resulting from the establishment of phase boundaries and their movement across the particle radius. It is noteworthy that this distribution of the state of lithiation at the surface and core of graphite particles is also present throughout the electrode thickness (Fig. S5). In contrast, despite the particle radius being larger for nC than for graphite (8.5  $\mu\text{m}$  vs 7.0  $\mu\text{m}$ , respectively), nC possesses intrinsically higher chemical diffusion coefficients and, more importantly, does not undergo phase separation during lithiation. These features enable faster diffusion and more homogeneous lithium distribution throughout the radius of nC particle (inset in Fig. 4B). Overall, this results in nC retaining more than 52% capacity at 2C compared to ca. 23% for graphite.

The capacity lost during fast-charge is highlighted in Fig. 4C and D, where the black line indicates the open circuit voltage (OCV, i.e., the quasi-equilibrium voltage during slow charge, see Fig. S4D) while the green line indicates the simulated voltage at 2C charge. The shaded areas between the two curves denote the breakdown of capacity loss contributions according to their physical and chemical origins, following the quantitatively fitted values from the modelling. By comparing model predictions for the two materials, we note that solid-state diffusion represents the highest contributor to capacity losses for most of the charge at 2C. In fact, both materials report solid-state diffusion as the dominant resistance (yellow region) as the charge proceeds.

Interestingly, as the charge approaches the voltage cut-off (i.e., below 0.1 V), the proportions of capacity losses in graphite change with a more prominent contribution provided by charge transfer (pink area in Fig. 4C), which ultimately becomes as limiting as the solid-state diffusion at the charge cut-off voltage of 0 V. In contrast, the proportion of nC contributions to capacity loss remains similar across the whole charge, with solid-state diffusion as the dominant contributor and only a marginal increase in charge transfer resistance close to the voltage cut-off (pink area Fig. 4D), albeit significantly lower than in graphite. Although improved charge transfer resistance in nC over graphite may stem from a difference in surface chemistry or SEI that enables favourable desolvation thermodynamics and kinetics for lithium-ions,<sup>44,45</sup> the main reason behind such different contributions lies in the different interplay between solid-state diffusion and charge transfer kinetics



in the two materials. As discussed above, nC possesses intrinsically higher chemical diffusion coefficients and, more importantly, does not undergo phase separation during lithiation. This results in a more homogeneous distribution of state of lithiation at the particle surface (see Fig. S5B), which gets saturated by intercalated lithium only at the end of the charge (state of lithiation ca. 0.86 at particle surface at 0 V, Fig. S5A) concurrently with the rise in charge transfer resistance; still, the local accumulation of intercalated lithium in nC is far from complete saturation. Graphite, instead, due to the phase separation phenomena, exhibits higher charge transfer resistances than nC because of the appearance of a lithium-rich phase (state of lithiation ca. 0.95, corresponding to stage 1) at particle surface much earlier during charge (compare the insets in Fig. 4A and B). This significantly increases the charge transfer resistance since the saturation of the particle surface slows down the intercalation reaction of lithium ions. Hence, the slow solid-state diffusion and the establishment of a stable lithium-rich phase at particle surface impede lithium intercalation, such that graphite shows a diffusion-induced increase in charge transfer resistance at the end of charge.

We note that the capacity loss due to electrolyte transport processes (in blue in Fig. 4C and D) may be systematically underestimated in this study compared to a situation where the anode is used in a full cell setup. This is due to the coin cell setup which ensures an excess inventory of electrolyte, so that electrolyte transport resistances across the separator and the Li metal counter electrode are neglected in the model (more details in the Methods section). Additionally, being the electrode thickness smaller for the graphite electrode than for nC (47.7  $\mu\text{m}$  vs 85.6  $\mu\text{m}$ , respectively, see Tab. S1) and given the lower areal capacity of the former, the capacity loss due to electrolyte transport is comparatively smaller in the graphite electrode (compare the blue areas in Fig. 4C and D). Overall, the results here highlight that multiple factors are bottlenecking fast-charge performance as opposed to a single limiting factor and that the nature of the active material has a profound effect on the charging rate performance<sup>44,45</sup>

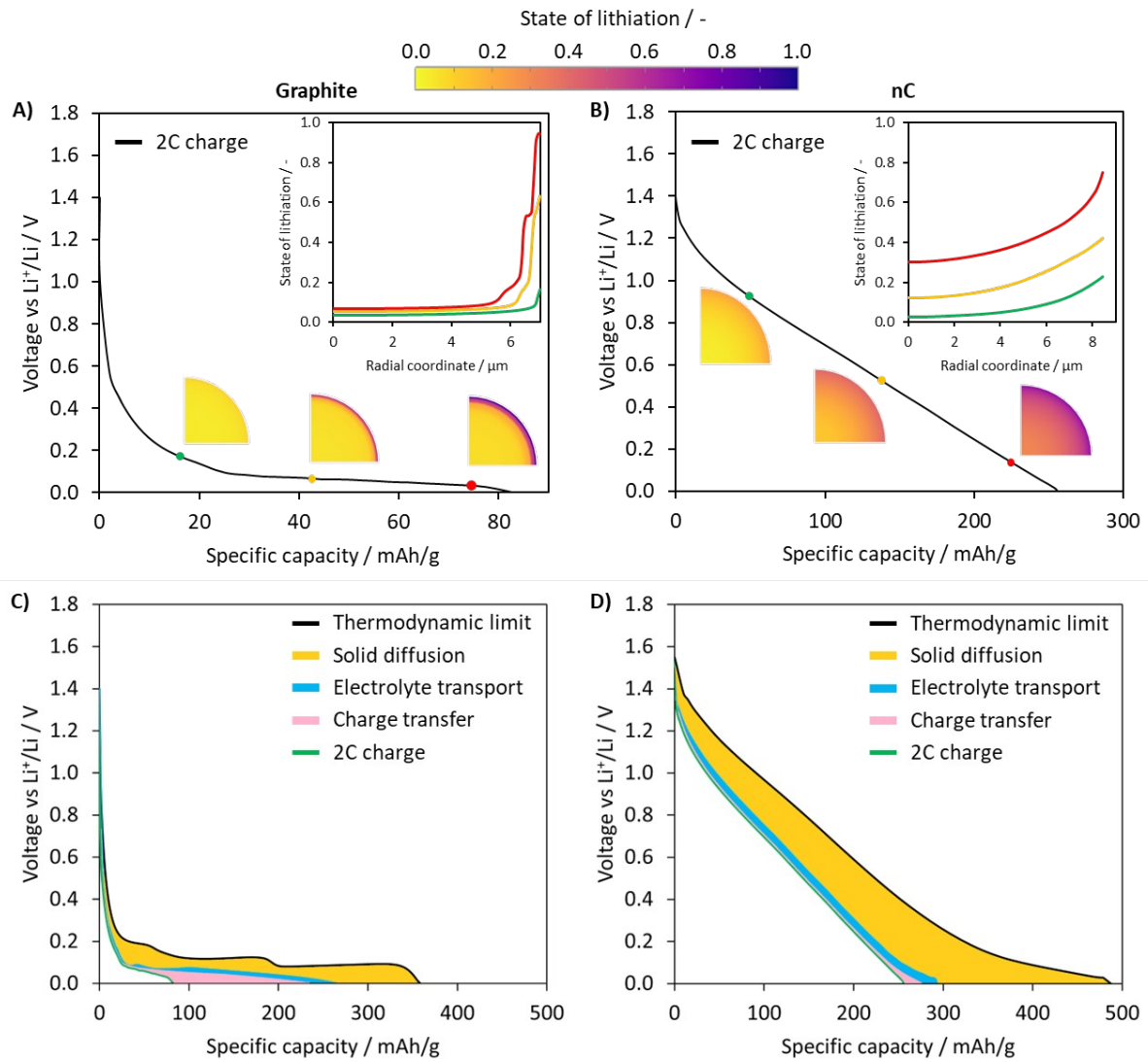


**Fig. 4.** Simulated galvanostatic charge curves at 2C, with inset visualisation of lithium distribution at a particle level for A) graphite and B) nC. The quarter circles depict the radial distribution of state of lithiation at different states of charge in a model secondary particle placed at the separator interface. Quantitative breakdown of capacity loss contributions during fast-charge identified by the model compared to the (near) thermodynamic limit for C) graphite and D) nC anode.

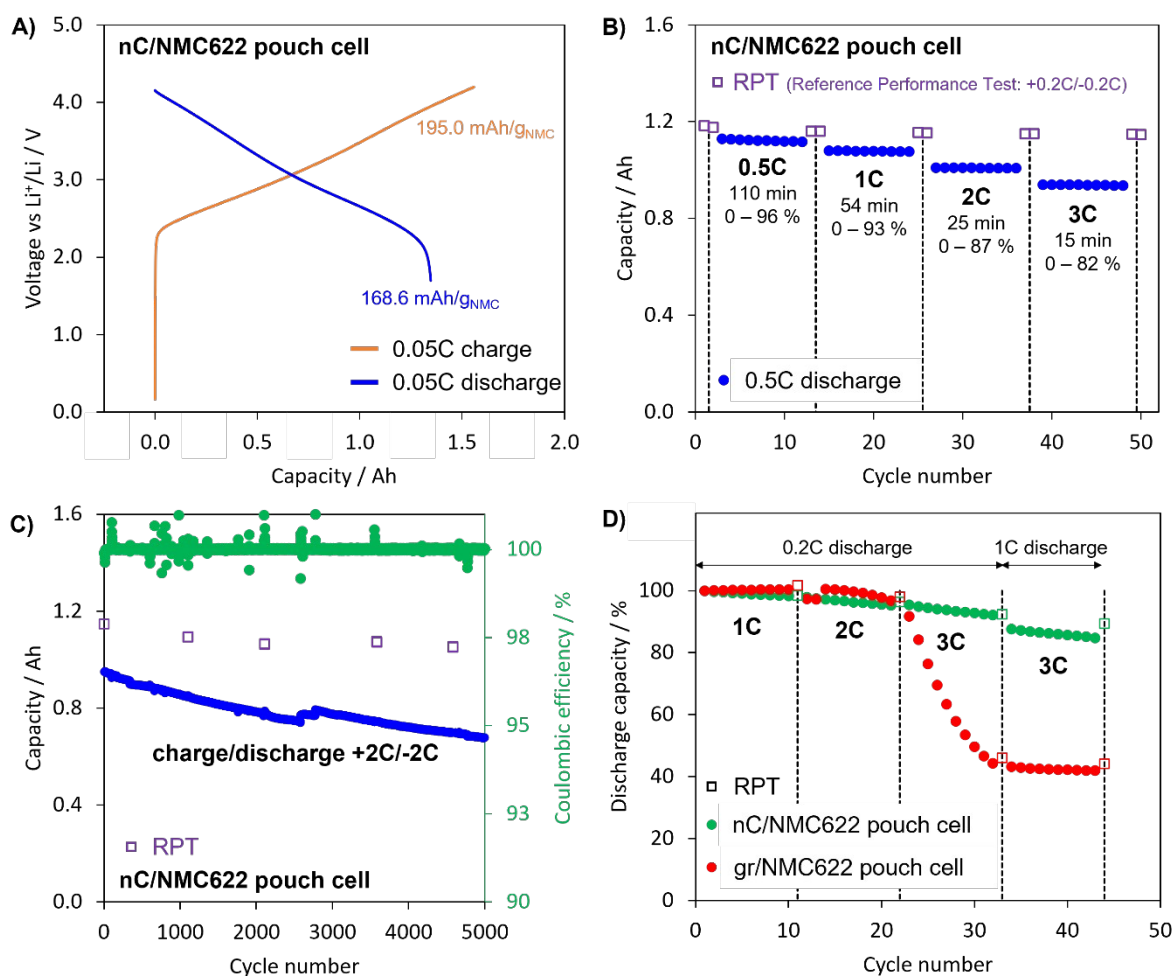


**Fig. 5.** A) Formation cycle of nC/NMC622 full multi-layer pouch cell. B) Charging rate performance for nC/NMC622 full multi-layer pouch cell at different charging C-rates (from 0.5C to 3C) and 0.5C discharge, with indication of state of charge ranges and charge duration. C) Capacity and coulombic efficiency, as a function of cycle number, for nC/NMC622 full multi-layer pouch cell cycled at 2C charge/2C discharge. D) Comparison of discharge capacity, as a function of cycle number, for graphite/NMC622 and nC/NMC622 full multi-layer pouch cells at different C-rates. In all the plots, RPT refers to reference performance tests performed at 0.2C.

The practical implications of cell and material level phenomena identified in half-cells and via computational modelling are demonstrated via cycling full multi-layer pouch cells;  $\text{LiNi}_{0.6}\text{Mn}_{0.2}\text{Co}_{0.2}\text{O}_2$  (NMC622) has been selected arbitrarily as cathode material and its weight proportion in the cell is 36% (average cell weight is 22 g; Fig. S6). Characteristic first charge/discharge cycle of built nC/NMC622 pouch cell is given in Fig. 5A, where specific capacities are calculated based on the mass of the cathode active material only. The coulombic efficiency during the formation cycle is 86%, implying that the initial capacity losses are 14%. nC demonstrates sloped voltage profile during charge/discharge, which is not unusual for disordered carbons and matches the voltage response in half-cell setup (Fig. 1B); at least at low C-rates, this has a rather negative impact on the cell energy due to overall lower nominal voltage (specific energies of  $185 \pm 5$  Wh/kg at cell level have been observed after formation).

Despite relatively high areal capacities of constituent electrodes, built prototype pouch cells display exceptionally high tolerance to repetitive fast charging even at ambient conditions, as shown in Fig. 5B. Both repetitive fast charging and Reference Performance Tests (RPT, performed at 0.2C) indicate little to no degradation during the rate capability test and therefore prolonged cycling experiments on 2C charge/2C discharge have been further carried out as well (Fig. 5C). RPT reveal that the accessible capacity at 0.2C does not change significantly over 5000 cycles (less than 10% capacity loss between the first and the last RPT in Fig. 5C), showing that there is no significant degradation or Li inventory loss. This observation agrees well with coulombic efficiency values close to 100%. Some decrease in capacity at higher C-rates over thousands of cycles are likely due to gradual increase in impedance (e.g., from the cathode side; ongoing work)<sup>46</sup> which results in the voltage limit being hit before full accessible capacity of the pouch cell can be reached.

Control experiments have been carried out with two batches of nC/NMC622 and artificial graphite/NMC622 identical multilayer pouch cells of close nominal capacities of around 2.3 Ah (Fig. 5D and Fig. S6). Early signs of fast-charge performance degradation for graphite appear at 2C charge step (see red dots in Fig. 5D) and severe irreversible capacity fading is observed during charge at 3C. Decreasing capacities point to significant growth of overpotentials and loss of inventory lithium, which likely has been plated onto the surface of graphite anode. This is in contrast with performance of nC full cells, which exhibit more stable fast-charge performance without significant degradation (green dots in Fig. 5D). Thus, nC offer some advantages as an anode material for fast-charge Li-ion cells, which may be used as either a standalone alternative active material or in combination with graphite blends in multi-layer anode architectures.<sup>47</sup>

## Conclusion

This study investigated the chemical origins of the lithiation mechanism in nanocluster disordered carbon materials and compared them against state-of-the-art artificial graphite. The findings confirm that solid-state lithium transport remains a significant obstacle limiting the high-rate charging capabilities of lithium-ion batteries, with the solid-state diffusion coefficient and the underlying physics of lithium-induced phase separation playing a critical role. The development of a novel multi-physics model that accounts for the effects of lithium intercalation via coupled ion electron transfer kinetics and non-ideal solid-state diffusion allowed for accurate modelling of the lithiation and, where present, phase separation mechanisms in graphitic and disordered carbon electrodes. Through model fitting, electrochemical tests, and material characterization of the two active materials, it was found that the solid-state diffusion in nanocluster carbon is greater than in graphite. The absence of phase separation and improved diffusion in nanocluster carbon allows better volume utilization, avoids the saturation of the active material particle's surface even at high charging rates, and effectively reduces the risk of plating. This translates into enhanced performance and higher capacity extraction compared to graphite. Furthermore, practical implications of nanocluster carbon were demonstrated through testing pouch cells, which showed remarkable results with coulombic efficiency close to 100% and less than 10% capacity loss over 5000 cycles at 2C. Disordered carbon-based pouch cells also demonstrated little degradation upon 3C fast-charge compared to graphite ones, where a severe irreversible capacity loss was detected. Overall, the results of this study provide new insights into the lithiation mechanisms of carbon-based anodes and highlight the potential of disordered carbon as an alternative to graphite for high-power applications. Further research and development of disordered carbon-based electrode materials

could lead to the design of more efficient and durable lithium-ion batteries capable of charging faster, facilitating the widespread adoption of electric vehicles and grid-scale energy storage systems.

## Materials and methods

### Materials

Synthetic graphite (BTR), Polyvinylidene fluoride (PVDF, Solef), C65 Carbon black (MTI), Carboxymethyl cellulose (CMC, Zeon), Styrene-Butadiene Rubber (SBR, Zeon), and N-methyl-2-pyrrolidone (anhydrous, Sigma-Aldrich) were used without further mechanical processing. Nanocluster carbon (nC),<sup>27</sup> a highly disordered form of carbon, was produced following an in-house method. Carbon based powders were dried for 12 hours in vacuum at 120 °C prior to slurry making.

### Electrode preparation

Negative electrode slurry composition of 92% active material, 4% carbon black and 4% binder was used. Graphite anode slurry based on PVDF and NMP was cast on 10 µm copper foil. Nanocluster carbon anode slurry based on CMC-SBR aqueous mixture was cast on 10 µm copper foil. Cast electrodes were dried in an air oven at 80 °C for 60 minutes prior to calendaring.

Positive electrodes have been prepared using  $\text{LiNi}_{0.6}\text{Mn}_{0.2}\text{Co}_{0.2}\text{O}_2$  (NMC622, BASF) as cathode active material, polyvinylidene fluoride (PVDF, Solef) as a binder and Super C65 carbon black as a conductive additive in a weight ratio of 96 : 2 : 2. The negative and positive electrodes have been up scaled to around 1 kg (anode) and 3 kg (cathode) slurry mixing batches for cells manufacturing. Prepared anodic and cathodic slurries have been casted on battery grade 10 µm copper and 15 µm aluminium foils respectively. Double sided negative and positive electrodes have been manufactured on a roll-to-roll coater, calendared up to optimal electrode densities (1.2 g/cm<sup>3</sup> for the anode and 3.2 g/cm<sup>3</sup> for the cathode) using a roll-press and slitted into 45x58 mm anodes and 45x56 mm cathodes. Target loadings for anode and cathode have been set to areal capacities around 3.6 and 3.0 mAh/cm<sup>2</sup> post formation respectively.

### X-ray diffraction measurements

Operando X-ray diffraction measurements were performed using a battery cell supplied by Rigaku equipped with an X-ray transparent aluminium-coated beryllium window. The active materials were incorporated into dry electrodes with polytetrafluoroethylene and Super C65 carbon black in a weight ratio 90 : 5 : 5, and then assembled into half cells versus Li metal. The electrode films were separated from the window by a 1 µm-thin Cu foil. The cell was mounted onto a Cu-source Rigaku 3kW SmartLab X-ray diffractometer equipped with a Ni Kβ filter and cycled at a rate of C/10.

### Cell construction

Symmetrical cells, GITT measurements and half-cell fast-charge measurements were conducted in coin-cells. Coin cells were constructed inside an Argon glovebox with < 1 ppm H<sub>2</sub>O and O<sub>2</sub>. Li metal chips (MTI) were brushed immediately before cell construction. Celgard 2235 was dried at 60 °C before cell construction. Calendared electrodes were cut and dried at 120 °C for 12 hours before cell construction. The electrolyte is 1M LiPF<sub>6</sub> in EC:DMC with 2% FEC.

Full cell measurements were conducted in multi-layer pouch cells. Prototype multilayer nC/NMC pouch cells of 1.3 Ah nominal capacity with stacked design (10 anodes / 9 cathodes with single layer 25  $\mu\text{m}$  Celgard 2500 polypropylene separators in between and enveloped into 120  $\mu\text{m}$  pouch film) have been assembled on a semi-automated pilot equipment and filled with 1M  $\text{LiPF}_6$  FEC/EMC (5/95 by vol.) 5 wt. % LiDFOB electrolyte solution taken in 3.3 g/Ah electrolyte-to-capacity ratio.

## Electrochemistry

Galvanostatic cycling has been performed by Neware CT4080T-5V6A-S1 multi-channel battery tester and Biologic VMP3. Temperature has been maintained by Binder MKFT 240 climate chamber and set at  $23 \pm 1^\circ\text{C}$ . During formation all cells have undergone three consecutive constant current charge/discharge cycles with current densities corresponding to C/20, voltage range of +0.002 to +1.5 V vs.  $\text{Li}^+/\text{Li}$  for graphite half cells, +0.002 to +2.5 V for nC half cells.

Full cells were formed in the voltage range of +1.7 to +4.2V, after which the pouch cells were degassed and resealed under vacuum. Tolerance towards fast charge has been estimated by rate capability tests at varying charging currents (0.5C, 1C, 2C and 3C) followed by 0.5C discharge after 10 min of rest. Prolonged cycling tests have been performed via constant current charge/discharge as 2C/2C with 10 min rest in between the steps. Cells degradation during the cycling has been assessed periodically via reference performance test (RPT) at 0.2C constant current charge / 0.2C constant current discharge.

Tortuosity of the electrodes were estimated by following a literature protocol based on construction of symmetrical coin cells.<sup>48</sup>

Galvanostatic intermittent titration technique used in the manuscript pulsed a current of ca. C/20 for 10 minutes followed by a rest period of 4 hours. Physical parameters associated with polarisation and relaxation were extracted by utilising a newly developed multi-physics model described below.

## Modelling and simulations

The electrochemical model developed in this study serves as a tool to evaluate kinetic and diffusion properties of graphite and nanocluster carbon as well as to quantify the contribution of activation, concentration and diffusion overpotential losses to the electrochemical response. The model solves mass and charge balances in a pseudo-2D (P2D) framework,<sup>49–52</sup> namely electron and electrolyte transport along the through-thickness 1D direction  $x$ , and solid-state diffusion of intercalated lithium along the 1D radial direction  $y$  in the active material particles. Model equations are solved only for the working electrode (i.e., graphite or nC), while the counter electrode (Li metal) and separator are assumed to be ideal (i.e., no concentration or activation losses in the separator and counter electrode) because Li metal has an excess capacity compared to the working electrode and there is a large inventory of electrolyte in the coin cell setup.

The model solves the electrolyte transport using concentrated solution theory,<sup>51–53</sup> while the charge transfer kinetics of lithium intercalation/de-intercalation is modelled via coupled ion electron transfer (CIET) kinetics.<sup>10,41</sup> Solid-state diffusion of intercalated lithium in the active material is modelled using the phase-field approach.<sup>40,54,55</sup> Originally developed for phase-separating materials,<sup>40,56,57</sup> the phase-field approach can also be used to model lithium transport in non-phase-

separating materials.<sup>43</sup> In this approach, the gradient of the chemical potential  $\mu$  of intercalated lithium governs its molar flux  $N_s$  within the active material, as follows:

$$N_s = \frac{-1}{RT} \bar{D}_s c_s \frac{\partial \mu}{\partial y} \quad (1)$$

where  $R$  is the universal gas constant,  $T$  is the temperature,  $c_s$  is the lithium molar concentration in the active material. Eq. (1) allows for accounting non-ideal solid-state diffusion, including uphill diffusion in phase-separating materials as well as the thermodynamic enhancement factor<sup>31,40,58</sup> for concentrated solid solutions. At open circuit conditions the lithium chemical potential  $\mu$  is related to open circuit voltage (OCV) via the Nernst equation  $U_{eq} = E^\circ - \frac{\mu}{F}$ ,<sup>42</sup> where  $U_{eq}$  is the OCV (which is a function of state of lithiation,  $\tilde{c}_s$ ),  $E^\circ$  is the standard potential of intercalated lithium, and  $F$  is the Faraday constant. Such an equilibrium relationship enables for reframing the molar flux in Eq. (1) in a Fick law form (i.e.,  $N_s = -D_s \frac{\partial c_s}{\partial y}$ ), where the chemical **diffusion coefficient**  $D_s$  can be computed from the intrinsic **diffusion coefficient**  $\bar{D}_s$  as:<sup>31,43</sup>

$$D_s = \bar{D}_s \frac{F}{RT} \tilde{c}_s \left( \frac{-\partial U_{eq}}{\partial \tilde{c}_s} \right) \quad (2)$$

The model, implemented in COMSOL Multiphysics, was calibrated and validated for both graphite and nC by using the experimental galvanostatic charge/discharge curves at different C-rates (Fig. 1A and B); for nC, also GITT data (Fig. 3A) were used for calibrating the **solid-state diffusion coefficient** and charge transfer kinetic constant. Model validation, along with an extended description of governing equations and parametrisation, can be found in the Supplementary Information.

## Acknowledgements

Grace Bridgewater, Michael Lain and Mark Copley from Warwick Manufacturing Group, University of Warwick are acknowledged for technical assistance in optimising the multi-layer full pouch cells. R.H. and D. C. thanks the Henry-Royce institute for funding under Royce ICP034. A.B. acknowledges funding from the European Union NextGenerationEU - National Recovery and Resilience Plan (NRRP) - MISSION 4 COMPONENT 2, INVESTMENT N. 1.3 - CUP N. I53C22001450006, within the project Network 4 Energy Sustainable Transition (NEST). This manuscript reflects only the authors' views and opinions, neither the European Union nor the European Commission can be considered responsible for them.

## References

1. Meintz, A. *et al.* Enabling fast charging – Vehicle considerations. *J Power Sources* **367**, 216–227 (2017).
2. Arora, P., White, R. E. & Doyle, M. Capacity Fade Mechanisms and Side Reactions in Lithium-Ion Batteries. *J Electrochem Soc* **145**, 3647–3667 (1998).

3. Son, S.-B. *et al.* Fast Charge-driven Li Plating on Anode and Structural Degradation of Cathode. *J Electrochem Soc* **167**, 140506 (2020).
4. Yang, X. G. *et al.* Asymmetric Temperature Modulation for Extreme Fast Charging of Lithium-Ion Batteries. *Joule* **3**, 3002–3019 (2019).
5. Wang, C. *et al.* Fast charging of energy-dense lithium-ion batteries. *Nature* (2022) doi:10.1038/s41586-022-05281-0.
6. Suthar, B., Northrop, P. W. C., Rife, D. & Subramanian, V. R. Effect of Porosity, Thickness and Tortuosity on Capacity Fade of Anode. *J Electrochem Soc* **162**, A1708–A1717 (2015).
7. Colclasure, A. M. *et al.* Electrode scale and electrolyte transport effects on extreme fast charging of lithium-ion cells. *Electrochim Acta* **337**, 135854 (2020).
8. Robertson, D. C. *et al.* Effect of Anode Porosity and Temperature on the Performance and Lithium Plating During Fast-Charging of Lithium-Ion Cells. *Energy Technology* **9**, (2021).
9. Grießl, D., Adam, A., Huber, K. & Kwade, A. Effect of the Slurry Mixing Process on the Structural Properties of the Anode and the Resulting Fast-Charging Performance of the Lithium-Ion Battery Cell. *J Electrochem Soc* **169**, 020531 (2022).
10. Gao, T. *et al.* Interplay of Lithium Intercalation and Plating on a Single Graphite Particle. *Joule* **5**, 393–414 (2021).
11. Bhandari, A. *et al.* Li nucleation on the graphite anode under potential control in Li-ion batteries. *J Mater Chem A Mater* **10**, 11426–11436 (2022).
12. Su, X. *et al.* Mechanisms for Lithium Nucleation and Dendrite Growth in Selected Carbon Allotropes. *Chemistry of Materials* **29**, 6205–6213 (2017).
13. Cao, W., Zheng, J., Adams, D., Doung, T. & Zheng, J. P. Comparative Study of the Power and Cycling Performance for Advanced Lithium-Ion Capacitors with Various Carbon Anodes. *J Electrochem Soc* **161**, A2087–A2092 (2014).
14. Fang, Y. *et al.* Lithium insertion in hard carbon as observed by <sup>7</sup>Li NMR and XRD. The local and mesoscopic order and their relevance for lithium storage and diffusion. *J Mater Chem A Mater* 10069–10082 (2022) doi:10.1039/d2ta00078d.
15. Xie, L. *et al.* Hard Carbon Anodes for Next-Generation Li-Ion Batteries: Review and Perspective. *Adv Energy Mater* **11**, 1–22 (2021).
16. Nagao, M. *et al.* Structure Characterization and Lithiation Mechanism of Nongraphitized Carbon for Lithium Secondary Batteries. *J Electrochem Soc* **153**, A914 (2006).
17. Dahn, J. R., Fong, R. & Spoon, M. J. Suppression of staging in lithium-intercalated carbon by disorder. *Phys Rev B* **42**, 6424–6432 (1990).
18. Yang, G. *et al.* Insights into lithium and sodium storage in porous carbon. *Nano Lett* **20**, 3836–3843 (2020).
19. Kizzire, D. G., Richter, A. M., Harper, D. P. & Keffer, D. J. Lithium and Sodium Ion Binding Mechanisms and Diffusion Rates in Lignin-Based Hard Carbon Models. *ACS Omega* **6**, 19883–19892 (2021).



20. Omichi, K. *et al.* Origin of Excess Irreversible Capacity in Lithium-Ion Batteries Based on Carbon Nanostructures. *J Electrochem Soc* **162**, A2106–A2115 (2015).
21. Larcher, D., Mudalige, C., Gharghouri, M. & Dahn, J. R. Electrochemical insertion of Li and irreversibility in disordered carbons prepared from oxygen and sulfur-containing pitches. *Electrochim Acta* **44**, 4069–4072 (1999).
22. Béguin, F. *et al.* A better understanding of the irreversible lithium insertion mechanisms in disordered carbons. *Journal of Physics and Chemistry of Solids* **65**, 211–217 (2004).
23. Guerin, K., Fevrier-Bouvier, A., Flandrois, S., Simon, B. & Biensan, P. On the irreversible capacities of disordered carbons in lithium-ion rechargeable batteries. *Electrochim Acta* **45**, 1607–1615 (2000).
24. Zhang, X. *et al.* Fast and Controllable Prelithiation of Hard Carbon Anodes for Lithium-Ion Batteries. *ACS Appl Mater Interfaces* **12**, 11589–11599 (2020).
25. Aravindan, V., Lee, Y. S. & Madhavi, S. Best Practices for Mitigating Irreversible Capacity Loss of Negative Electrodes in Li-Ion Batteries. *Adv Energy Mater* **7**, 1–17 (2017).
26. Shen, Y., Qian, J., Yang, H., Zhong, F. & Ai, X. Chemically Prelithiated Hard-Carbon Anode for High Power and High Capacity Li-Ion Batteries. *Small* **16**, 1–7 (2020).
27. Gurevich, S. *et al.* A SUB-CRITICAL NUCLEATION PROCESS FOR MAKING STABLE CLUSTERS OF ATOMS THAT ARE OF SUBCRITICAL SIZE, AND THE STRUCTURE, PROPERTIES AND APPLICATIONS OF MATERIALS THAT ARE MADE FROM THESE CLUSTERS BACKGROUND OF THE INVENTION. (2020).
28. Missyul, A., Bolshakov, I. & Shpanchenko, R. XRD study of phase transformations in lithiated graphite anodes by Rietveld method. *Powder Diffr* **32**, S56–S62 (2017).
29. Jiang, Y., Niu, Z., Offer, G., Xuan, J. & Wang, H. Insights into the Role of Silicon and Graphite in the Electrochemical Performance of Silicon/Graphite Blended Electrodes with a Multi-Material Porous Electrode Model. *J Electrochem Soc* **169**, 020568 (2022).
30. Smith, R. B. & Bazant, M. Z. Multiphase Porous Electrode Theory. *J Electrochem Soc* **164**, E3291–E3310 (2017).
31. Weppner, W. & Huggins, R. A. Determination of the Kinetic Parameters of Mixed-Conducting Electrodes and Application to the System Li<sub>3</sub>Sb. *J Electrochem Soc* **124**, 1569–1578 (1977).
32. Honders, A., der Kinderen, J. M., van Heeren, A. H., de Wit, J. H. W. & Broers, G. H. J. Bounded diffusion in solid solution electrode powder compacts. Part II. The simultaneous measurement of the chemical diffusion coefficient and the thermodynamic factor in Li<sub>x</sub>TiS<sub>2</sub> and Li<sub>x</sub>CoO<sub>2</sub>. *Solid State Ion* **15**, 265–276 (1985).
33. Deiss, E. Spurious chemical diffusion coefficients of Li<sup>+</sup> in electrode materials evaluated with GITT. *Electrochim Acta* **50**, 2927–2932 (2005).
34. Horner, J. S. *et al.* Electrochemical Modeling of GITT Measurements for Improved Solid-State Diffusion Coefficient Evaluation. *ACS Appl Energy Mater* **4**, 11460–11469 (2021).
35. Markevich, E., Levi, M. D. & Aurbach, D. Comparison between potentiostatic and galvanostatic intermittent titration techniques for determination of chemical diffusion coefficients in ion-insertion electrodes. *Journal of Electroanalytical Chemistry* **580**, 231–237 (2005).

36. Han, B. C., Van Der Ven, A., Morgan, D. & Ceder, G. Electrochemical modeling of intercalation processes with phase field models. *Electrochim Acta* **49**, 4691–4699 (2004).
37. Kang, S. D. & Chueh, W. C. Galvanostatic Intermittent Titration Technique Reinvented: Part I. A Critical Review. *J Electrochem Soc* **168**, 120504 (2021).
38. Kang, S. D. *et al.* Galvanostatic Intermittent Titration Technique Reinvented: Part II. Experiments. *J Electrochem Soc* **168**, 120503 (2021).
39. Ruess, R. *et al.* Influence of NCM Particle Cracking on Kinetics of Lithium-Ion Batteries with Liquid or Solid Electrolyte. *J Electrochem Soc* **167**, 100532 (2020).
40. Bazant, M. Z. Theory of chemical kinetics and charge transfer based on nonequilibrium thermodynamics. *Acc Chem Res* **46**, 1144–1160 (2013).
41. Fraggedakis, D. *et al.* Theory of coupled ion-electron transfer kinetics. *Electrochim Acta* **367**, (2021).
42. Smith, R. B., Khoo, E. & Bazant, M. Z. *Intercalation Kinetics in Multiphase Layered Materials*. *J. Phys. Chem. C, Just Accepted Manuscript • Publication Date* <http://pubs.acs.org> (2017).
43. Horner, J. S. *et al.* Electrochemical Modeling of GITT Measurements for Improved Solid-State Diffusion Coefficient Evaluation. *ACS Appl Energy Mater* **4**, 11460–11469 (2021).
44. Keefe, A. S., Buteau, S., Hill, I. G. & Dahn, J. R. Temperature Dependent EIS Studies Separating Charge Transfer Impedance from Contact Impedance in Lithium-Ion Symmetric Cells. *J Electrochem Soc* **166**, A3272–A3279 (2019).
45. Jow, T. R., Delp, S. A., Allen, J. L., Jones, J.-P. & Smart, M. C. Factors Limiting Li + Charge Transfer Kinetics in Li-Ion Batteries. *J Electrochem Soc* **165**, A361–A367 (2018).
46. Strehle, B., Friedrich, F. & Gasteiger, H. A. A Comparative Study of Structural Changes during Long-Term Cycling of NCM-811 at Ambient and Elevated Temperatures. *J Electrochem Soc* **168**, 050512 (2021).
47. Hamed, A.-S. *et al.* Multi-layer anodes for high-current applications. *Electrochimica Acta* **439**, 141649 (2023).
48. Landesfeind, J., Hattendorff, J., Ehrl, A., Wall, W. A. & Gasteiger, H. A. Tortuosity Determination of Battery Electrodes and Separators by Impedance Spectroscopy. *J Electrochem Soc* **163**, A1373–A1387 (2016).
49. Cai, L. & White, R. E. Mathematical modeling of a lithium ion battery with thermal effects in COMSOL Inc. Multiphysics (MP) software. *J Power Sources* **196**, 5985–5989 (2011).
50. Torchio, M., Magni, L., Gopaluni, R. B., Braatz, R. D. & Raimondo, D. M. LIONSIMBA: A Matlab Framework Based on a Finite Volume Model Suitable for Li-Ion Battery Design, Simulation, and Control. *J Electrochem Soc* **163**, A1192–A1205 (2016).
51. Lagnoni, M., Nicolella, C. & Bertei, A. Survey and sensitivity analysis of critical parameters in lithium-ion battery thermo-electrochemical modeling. *Electrochim Acta* **394**, (2021).
52. Newman, J. & Tiedemann, W. Porous-electrode theory with battery applications. *AIChE* **21**, 25–45 (1975).

53. Fuller, T. F., Doyle, M. & Newman, J. *ELECTROCHEMICAL SCIENCE AND TECHNOLOGY Simulation and Optimization of the Dual Lithium Ion Insertion Cell*. *J. Electrochem. Soc* vol. 141 (1994).
54. Horner, J. S. *et al.* Electrochemical Modeling of GITT Measurements for Improved Solid-State Diffusion Coefficient Evaluation. *ACS Appl Energy Mater* **4**, 11460–11469 (2021).
55. Thomas-Alyea, K. E., Jung, C., Smith, R. B. & Bazant, M. Z. In Situ Observation and Mathematical Modeling of Lithium Distribution within Graphite. *J Electrochem Soc* **164**, E3063–E3072 (2017).
56. Singh, G. K., Ceder, G. & Bazant, M. Z. Intercalation dynamics in rechargeable battery materials: General theory and phase-transformation waves in LiFePO<sub>4</sub>. *Electrochim Acta* **53**, 7599–7613 (2008).
57. Bazant, M. Z. Thermodynamic stability of driven open systems and control of phase separation by electro-autocatalysis. *Faraday Discuss* **199**, 423–463 (2017).
58. Lai, W. & Ciucci, F. Mathematical modeling of porous battery electrodes-Revisit of Newman's model. *Electrochim Acta* **56**, 4369–4377 (2011).